



**ENABLING TECHNOLOGIES FOR  
CELL-BASED CLINICAL TRANSLATION**

# CRISPR/Cas9-mediated introduction of the sodium/iodide symporter gene enables noninvasive in vivo tracking of induced pluripotent stem cell-derived cardiomyocytes

John W. Ostrominski<sup>1</sup> | Ravi Chandra Yada<sup>1</sup> | Noriko Sato<sup>2</sup> | Michael Klein<sup>3</sup> | Ksenia Blinova<sup>4</sup> | Dakshesh Patel<sup>4</sup> | Racquel Valadez<sup>5</sup> | Maryknoll Palisoc<sup>5</sup> | Stefania Pittaluga<sup>5</sup> | Kah-Whye Peng<sup>6</sup> | Hong San<sup>7</sup> | Yongshun Lin<sup>8</sup> | Falguni Basuli<sup>9</sup> | Xiang Zhang<sup>9</sup> | Rolf E. Swenson<sup>9</sup> | Mark Haigney<sup>3</sup> | Peter L. Choyke<sup>2</sup> | Jizhong Zou<sup>8</sup> | Manfred Boehm<sup>10</sup> | So Gun Hong<sup>1</sup>  | Cynthia E. Dunbar<sup>1</sup> 

<sup>1</sup>Translational Stem Cell Biology Branch, National Heart, Lung and Blood Institute (NHLBI), National Institutes of Health (NIH), Bethesda, Maryland

<sup>2</sup>Molecular Imaging Program, Laboratory of Cellular Therapeutics, National Cancer Institute (NCI), NIH, Bethesda, Maryland

<sup>3</sup>Division of Cardiology, Uniformed Services University of the Health Sciences, Bethesda, Maryland

<sup>4</sup>Office of Science and Engineering Laboratories, Center for Devices and Radiological Health, US Food and Drug Administration, Silver Spring, Maryland

<sup>5</sup>Laboratory of Pathology, Center for Cancer Research, NCI, NIH, Bethesda, Maryland

<sup>6</sup>Department of Molecular Medicine, Mayo Clinic, Rochester, Minnesota

<sup>7</sup>Animal Surgery and Resources Core, NHLBI, NIH, Bethesda, Maryland

<sup>8</sup>iPSC Core, NHLBI, NIH, Bethesda, Maryland

<sup>9</sup>Chemistry and Synthesis Center, NHLBI, NIH, Bethesda, Maryland

<sup>10</sup>Laboratory of Cardiovascular Regenerative Medicine, NHLBI, NIH, Bethesda, Maryland

**Correspondence**

Cynthia E. Dunbar, MD, and So Gun Hong, DVM, PhD, National Heart, Lung, and Blood Institute, National Institutes of Health,

**Abstract**

Techniques that enable longitudinal tracking of cell fate after myocardial delivery are imperative for optimizing the efficacy of cell-based cardiac therapies. However, these approaches have been underutilized in preclinical models and clinical trials, and there is considerable demand for site-specific strategies achieving long-term expression of reporter genes compatible with safe noninvasive imaging. In this study, the rhesus sodium/iodide symporter (NIS) gene was incorporated into rhesus macaque induced pluripotent stem cells (RhiPSCs) via CRISPR/Cas9. Cardiomyocytes derived from NIS-RhiPSCs (NIS-RhiPSC-CMs) exhibited overall similar morphological and electrophysiological characteristics compared to parental control RhiPSC-CMs at baseline and with exposure to physiological levels of sodium iodide. Mice were injected intramyocardially with 2 million NIS-RhiPSC-CMs immediately following myocardial infarction, and serial positron emission tomography/computed tomography was performed with <sup>18</sup>F-tetrafluoroborate to monitor transplanted cells in vivo. NIS-RhiPSC-CMs could be detected until study conclusion at 8 to 10 weeks postinjection. This NIS-based molecular imaging platform, with optimal safety and sensitivity characteristics, is primed for translation into large-animal preclinical models and clinical trials.

**KEYWORDS**

cardiomyocytes, CRISPR/Cas9, electrophysiology, imaging, in vivo tracking, iPSCs, NIS, PET, rhesus macaque, sodium iodide symporter

John W. Ostrominski and Ravi Chandra Yada contributed equally to this study.

This is an open access article under the terms of the Creative Commons Attribution-NonCommercial-NoDerivs License, which permits use and distribution in any medium, provided the original work is properly cited, the use is non-commercial and no modifications or adaptations are made.

© 2020 The Authors. STEM CELLS TRANSLATIONAL MEDICINE published by Wiley Periodicals LLC on behalf of AlphaMed Press.

Bethesda, MD 20892.

Email: [dunbarc@nhlbi.nih.gov](mailto:dunbarc@nhlbi.nih.gov) (C. E. D.) and [sogun.hong@nih.gov](mailto:sogun.hong@nih.gov) (S. H.)

#### Funding information

Medical Research Scholars Program of the NIH; Division of Intramural Research program of the NHLBI and NCI

## 1 | INTRODUCTION

Imaging approaches enabling noninvasive longitudinal monitoring of cardiac cellular therapies are imperative for assessment of the safety and efficiency endpoints required for clinical translation, including engraftment, persistence, localization, and correlation with functional and structural outcomes. However, applicable long-term cell tracking technologies are lacking, particularly for application in relevant immunocompetent large animal models, where approaches using optical scanning of xenogeneic fluorescent proteins are not applicable.<sup>1</sup> The sodium/iodide symporter (NIS), a transmembrane protein expressed normally at high levels in the thyroid and stomach, but with limited expression in other tissues,<sup>2</sup> has many advantageous properties for in vivo cell fate tracking. NIS is nonimmunogenic and allows multimodality molecular imaging with various safe and clinically available radiotracers. Furthermore, NIS has been shown to enable sensitive and specific in vivo identification of transplanted cells in the injured heart via radiolabeled substrate injection followed by either positron emission tomography (PET) or single-photon emission computed tomography.<sup>3-5</sup> However, these prior studies suffer from issues that could impede translation to the clinic, such as reliance upon clinically irrelevant donor cell types, inefficient plasmid transfection, use of nonintegrating adenoviral vectors offering only transient expression, or application of potentially genotoxic or silenced lentiviral vectors to introduce the NIS gene. In addition, there has been limited assessment of the effect of NIS expression on cardiomyocyte physiology. Hence, development of strategies that use site-specific gene introduction methods offering safe and durable transgene expression would overcome these limitations, accelerating utilization of in vivo imaging techniques.

We have previously used CRISPR/Cas9 targeted genome editing to introduce transgenes into the adeno-associated virus site 1 (AAVS1) safe harbor locus in rhesus macaque induced-pluripotent stem cells (RhiPSCs), a site known to enable robust and stable gene expression in both pluripotent and differentiated cells, while minimizing genotoxicity.<sup>6,7</sup> We now report the utility of this genome targeting approach to introduce the NIS gene into RhiPSCs at the AAVS1 site, and demonstrate the feasibility and relevance of this model to the preclinical development of regenerative cardiac therapies. In addition, for the first time, we present a thorough and clinically oriented electrophysiological (EP) description of NIS-positive induced pluripotent stem cell-derived cardiomyocytes (iPSC-CMs). RhiPSCs were selected for this study as they, unlike human iPSCs (hiPSCs), have the additional advantage of being directly compatible with long-term preclinical studies in clinically relevant nonhuman primate (NHP) large animal

### Significance statement

In vivo imaging techniques are imperative to guide clinical translation of cell-based therapeutics; however, current strategies are limited by immunogenicity and potential genotoxicity. In this proof-of-principle study, site-specific delivery of the sodium/iodide symporter (NIS) gene via CRISPR/Cas9 enabled sensitive in vivo tracking of induced pluripotent stem cell-derived cardiomyocytes (iPSC-CM) in a clinically relevant model of myocardial infarction, and NIS-positive iPSC-CMs retained electrophysiological characteristics comparable to controls. Featuring a superior safety profile, this approach offers wider applications in both the preclinical and clinical development of cardiac cell therapies.

models. RhiPSCs resemble hiPSCs in terms of colony morphology, expression of pluripotency-associated transcription factors and surface markers, and are dependent on similar growth factors to maintain their pluripotency.<sup>8,9</sup> In addition, RhiPSCs and hiPSCs have been shown to confer comparable cardioprotection in another rodent model of myocardial infarction, and via similar mechanisms.<sup>10</sup> Moreover, NHPs bear key anatomical, physiological, and immunologic similarities to humans that would enable closer translation of strategies that optimize therapeutic efficacy. In this regard, we describe a new NIS-based platform that has the potential to greatly enhance utilization of molecular imaging techniques in both preclinical and clinical trials of regenerative cardiac cell therapies.

## 2 | MATERIALS AND METHODS

### 2.1 | Animal use

All animals used in this study were housed and handled in accordance with protocols approved by the Institutional Animal Care and Use Committees of the NHLBI and NCI.

### 2.2 | RhiPSC generation and maintenance

Rhesus CD34<sup>+</sup> hematopoietic stem and progenitor cells or skin fibroblasts were isolated and reprogrammed as previously described.<sup>6,11,12</sup> RhiPSCs were cultured either on mouse embryonic fibroblast

(GlobalStem) feeders or growth factor-reduced Matrigel (BD Biosciences)-coated plates.

### 2.3 | Generation of NIS-RhiPSCs via CRISPR/Cas9-mediated genomic editing

The rhesus NIS transgene was removed from the pLV-SFFV-NIS-PGK-Puro plasmid (Imanis Life Sciences) via digestion with restriction enzymes BamHI and NotI, and cloned into the rhesus AAVS1-CAG-copGFP donor plasmid (Addgene #84209). The all-in-one CRISPR/Cas9 vector containing the high-fidelity eSpCas9 (Addgene #79145), the previously reported rhesus AAVS1 guide RNA sequence, and the NIS donor plasmid were introduced into RhiPSCs via nucleofection, and puromycin selection was performed to enrich targeted cells (Figure 1A).<sup>6,13</sup> Clones with NIS integration at the intended rhesus AAVS1-like site were identified as previously described.<sup>6,13</sup>

### 2.4 | Teratoma assay

Standard teratoma assays to document pluripotency were conducted using NIS-positive and control parental RhiPSCs in nonobese diabetic severe combined immunodeficient *Il2rg*<sup>-/-</sup> (NSG) mice (Jackson Laboratories) as described.

### 2.5 | In vitro function of NIS

In vitro substrate transport function of NIS-positive RhiPSCs was determined using <sup>18</sup>F-tetrafluoroborate (<sup>18</sup>F-TFB). Cells cultured on Matrigel were dissociated with Accutase (STEMCELL Technologies) and  $1 \times 10^6$  cells were resuspended in 500  $\mu$ L of either uptake buffer, 10 mM 4-(2-hydroxyethyl)-1-piperazineethanesulfonic acid (HEPES) in 1x Hanks' Balanced Salt Solution (HEPES/HBSS, Thermo Fisher Scientific) or inhibitor buffer, 10 mM HEPES/HBSS supplemented with 2 mM potassium perchlorate (KClO<sub>4</sub>). <sup>18</sup>F-TFB (1.11 MBq, 30  $\mu$ Ci) was added to the cell suspension and allowed to incubate for 1 hour at 37°C. Following incubation, cells were washed three times with 10 mM HEPES/HBSS and the residual radioactivity within the pellet was quantitated via  $\gamma$ -counter (Wizard2 Automatic Gamma Counter; Perkin Elmer) in counts per minute (CPM). As a radioactivity standard, one tenth of the activity used for the assay (111 kBq, 3  $\mu$ Ci) was added to three empty tubes and measured in parallel with the cell samples 1 hour later. The activity taken up by the cells was decay corrected to the starting time of the incubation to minimize experiment-to-experiment decay differences occurred between the start of the assay and activity measurement. Decay-corrected incorporated activity (kBq) of each sample was derived by dividing its CPM with the mean CPM of the standards, and then multiplied by 111 (kBq). In Figures 1 and 3, decay-corrected incorporated activity per million cells was expressed as kBq.

## 2.6 | Cardiac differentiation

Cardiac differentiation of RhiPSCs was performed as previously described.<sup>12</sup> Briefly, RhiPSCs were dissociated and cultured with Activin A (10 ng/mL, R&D), bone morphogenic protein 4 (BMP4; 10 ng/mL, R&D), and fibroblast growth factor 2 (FGF2; 10 ng/mL, Peprotech) for 3 days. Wnt signaling inhibitor IWP2 (3  $\mu$ M, Tocris) was then added for an additional 5 days. Following differentiation, cells were maintained in insulin (20  $\mu$ g/mL, Sigma)-containing medium for further maturation.

## 2.7 | Immunohistochemistry

Cells were fixed in 2% paraformaldehyde (PFA) in phosphate-buffered saline (PBS) for 30 minutes, followed by incubation in blocking buffer (PBS + 4% bovine serum albumin) for 30 minutes. Fixed cells were then incubated with primary antibody followed by incubation with a fluorescently labeled secondary antibody, each for 1 hour at room temperature. Last, 4',6-diamidino-2'-phenylindole dihydrochloride (DAPI) was applied to labeled cells and allowed to incubate for 10 minutes. Specific primary antibodies and dilutions used were: antibodies against human NIS (rabbit, 1:200, Imanis Life Sciences), CTnT (cardiac troponin T; mouse, 1:1000, DSHB),  $\alpha$ -actinin (mouse, 1:1000, Sigma), and NKX2.5 (mouse, 1:200, Abcam). Secondary labeling was performed with an anti-rabbit Alexa Fluor 555 (1:1000, Thermo Fisher Scientific) or an anti-mouse Alexa Fluor 488 (1:1000, Thermo Fisher Scientific).

## 2.8 | Patch clamp

RhiPSC-CMs were dissociated and plated onto glass coverslips as single cells as previously described.<sup>12</sup> For action potential (AP) measurements, cells were inserted into a small-volume chamber and bathed in Tyrode's solution (140 mM NaCl, 5.4 mM KCl, 1.8 mM CaCl<sub>2</sub>, 1.0 mM MgCl<sub>2</sub>, 10 mM HEPES, 10 mM glucose, pH 7.4) and maintained at 33°C to 35°C. Spontaneous and evoked APs were recorded using a patch clamp amplifier (Axopatch 200B, Molecular Devices) in whole-cell current-clamp mode. Pipettes (1-3 M $\Omega$ ) were filled with a standard internal solution. Calcium (Ca<sup>2+</sup>) transients were simultaneously measured as previously described,<sup>12</sup> using a fluorescent Ca<sup>2+</sup> indicator (Cal-520, AAT-Bioquest). Recorded fluorescence was corrected for background and normalized to the baseline value ( $\Delta F/F_0$ ). In some cases, recordings were performed 3 minutes after addition of sodium iodide (NaI), in which 10% of the well medium was replaced with a 10x concentrated NaI stock solution warmed to 37°C, yielding a final concentration of 1 mM NaI.

## 2.9 | Optical imaging

AP parameters of RhiPSC-CMs were measured as described.<sup>14</sup> Briefly, RhiPSC-CMs were plated onto 96-well glass-bottom plates (MatTek,

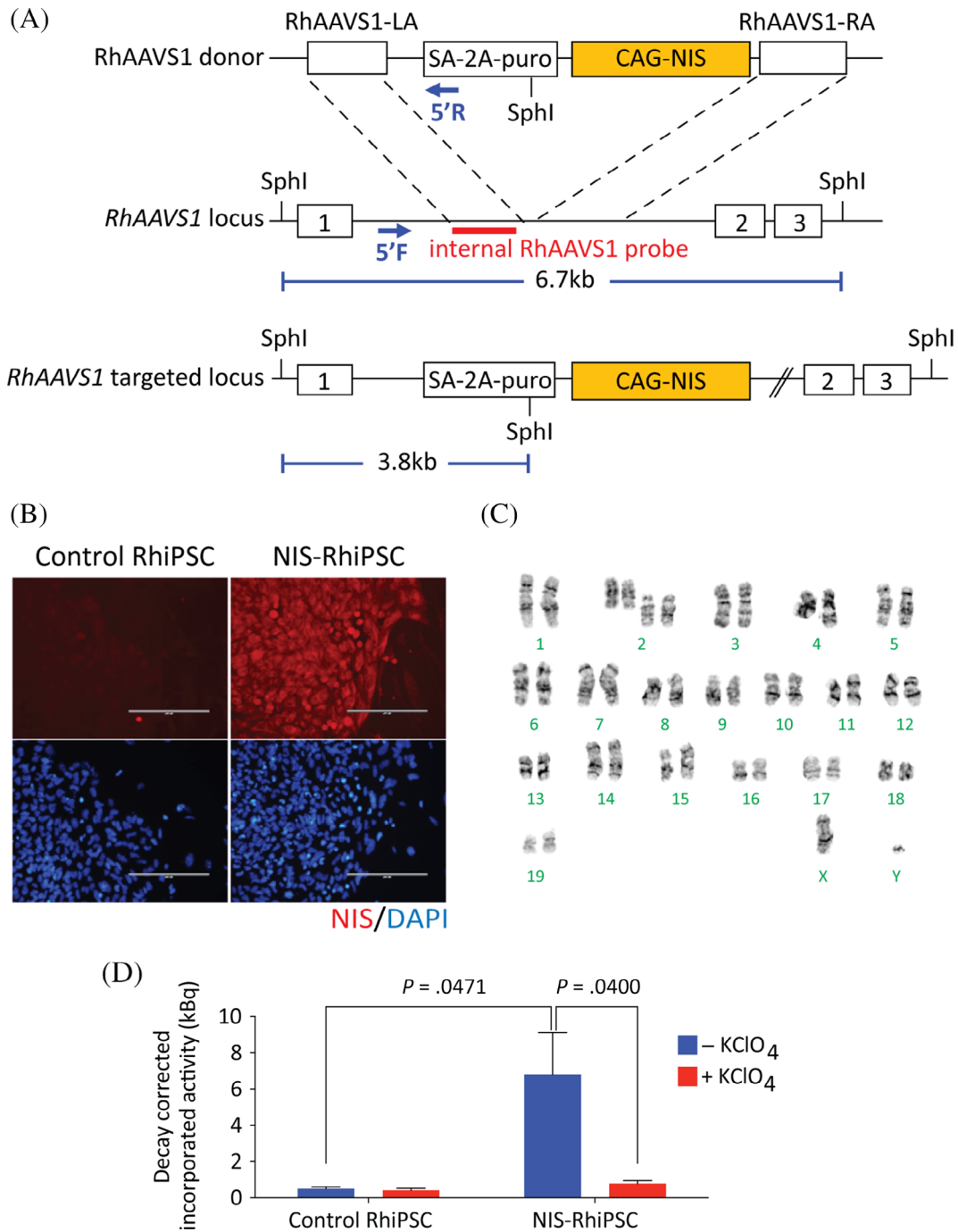


**FIGURE 1** Functional NIS expression in NIS-RhiPSCs. A, Schematic of the NIS donor plasmid construct (RhAAVS1-CAG-RhNIS) and the AAVS1 target site in the rhesus genome (*RhAAVS1*) between exons 1 and 2. The donor plasmid contains RhAAVS1 left (LA) and right (RA) homology arms flanking an excisable puromycin selection cassette and the RhNIS cDNA driven by a CAG promoter. B, Immunostaining confirmed expression of RhNIS (red) in NIS-RhiPSCs, compared to no expression in parental RhiPSCs. Counterstaining with DAPI (blue) reveals ~100% RhNIS positivity in cultured NIS-RhiPSCs. Scale bar = 200 μm. C, Karyotype NIS-RhiPSCs retained normal. D, Uptake assay showing functionality of RhNIS in NIS-RhiPSCs. Statistical analysis of in vitro <sup>18</sup>F-TFB uptake between NIS-positive (n = 7) and control cells (n = 5), without KClO<sub>4</sub> was performed with a *t* test for independent samples. Statistical analysis of in vitro <sup>18</sup>F-TFB uptake in NIS-positive cells, with and without KClO<sub>4</sub> (n = 7) was performed with a paired *t* test. Error bars represent mean ± SEM. <sup>18</sup>F-TFB, <sup>18</sup>F-tetrafluoroborate; AAVS1, adeno-associated virus site 1; DAPI, 4',6-diamidino-2-phenylindole dihydrochloride; RhiPSCs, rhesus macaque induced pluripotent stem cells

P96G-1.5-5-F) precoated with Matrigel at  $1 \times 10^5$  cells per well. The effects of Nal on AP parameters were studied 2 to 5 days after plating, or on days 15 to 20 of cardiac differentiation. On the day of the

testing, RhiPSC-CMs maintenance medium was replaced with optically transparent Dulbecco's Modified Eagle Medium (FluoroBrite, Thermo Fisher Scientific) and cells were stained with 6 μM di-4-



ANEPPS (Thermo Fisher Scientific) for 1 minute and allowed to re-equilibrate in dye-free FluoroBrite at 37°C, 5% CO<sub>2</sub> for 2 hours before baseline recordings. Spontaneous RhiPSC-CM APs were measured using ratiometric fluorescence recordings by a plate-based optical system (CelloPTIQ, Clyde Biosciences). AP recordings of 20-second duration were obtained from each well at baseline and 45 minutes after Nal addition. Each dose of Nal was assessed in multiple wells ( $n \geq 10$ ) by replacing 10% of the well medium with 10x concentrated Nal stock solution warmed to 37°C. Vehicle controls (Nal-free medium) were included on each plate ( $n \geq 10$ ). The Fridericia formula was used to calculate the AP duration corrected for the beating rate (APD<sub>C</sub>). Rate-corrected baseline and vehicle-controlled Nal-induced changes in AP duration at 90% repolarization were calculated ( $\Delta\Delta\text{APD}_{90\text{C}}$ ).

## 2.10 | Induction of myocardial infarction and intramyocardial cell injection

Myocardial infarction in 3-month-old NSG mice was induced via 90-minute ligation of the left anterior descending (LAD) coronary artery, followed by reperfusion.  $2 \times 10^6$  NIS-RhiPSC-CMs in 30  $\mu\text{L}$  pro-survival media consisting of 50% 10  $\mu\text{M}$  ROCK inhibitor in maintenance medium and 50% Matrigel were injected into the myocardium at the border zone of the infarct area immediately prior to reperfusion. Control injections consisted only of vehicle.

## 2.11 | Animal imaging and analysis

<sup>18</sup>F-TFB was synthesized in a radiochemical yield of 18% to 50% ( $n = 50$ , uncorrected for decay) and greater than 99% radiochemical purity, on par with other preclinical and clinical studies<sup>15-17</sup> in which <sup>18</sup>F-TFB was used. All animal imaging was performed using microPET/computed tomography imager ( $\mu\text{PET}/\text{CT}$ ; BioPET, Bioscan), and images were acquired 1 hour after intravenous injection of 3.7 MBq <sup>18</sup>F-TFB. An optimal wait time of 60 minutes was chosen based on a preliminary study, wherein superior visualization of NIS-RhiPSC-derived cells was achieved compared with imaging at 90 minutes. A 250 to 700 keV energy window was used, and 5-minute emission scans per bed position for a total of two bed positions were acquired. The acquired PET images were reconstructed using a three-dimensional ordered-subsets expectation maximization (3D OSEM) algorithm. PET images reconstructed using a 2D OSEM algorithm were analyzed using MiM (MiM Software, Inc.) for image quantitation. Regions of interest were drawn at the boundary of signal at each teratoma or implanted cells at the heart on axial images, and both volumetric and radioactivity information was recorded. VivoQuant (Build 3.0, Invicro) was used to merge maximum intensity projection PET images and CT. The total lesion <sup>18</sup>F-TFB uptake, which is equivalent to total lesion glycolysis in <sup>18</sup>F-fluorodeoxyglucose imaging, was calculated by multiplying the volume of lesion with increased <sup>18</sup>F-TFB uptake (mL) and its mean standardized uptake value (SUV). The total lesion <sup>18</sup>F-TFB

uptake is a normalized value taking into account both the injected dose and body weight of the mouse.

## 2.12 | Histological analysis

For immunohistochemical analysis on frozen sections of explanted murine tissues, samples were fixed with 4% PFA and blocked in 3% goat serum. All primary and secondary antibodies and their respective concentrations were used as above in the immunohistochemistry section, with the sole exception of CTnT, which was concentrated to 1:200. Detection was performed via Ventana Benchmark XT (Ventana Medical Systems) using the UltraView DAB Detection Kit. NIS-immunostained slides were analyzed by MetaMorph software.

## 2.13 | Statistical analysis

The Student's *t* test was used to compare in vitro <sup>18</sup>F-TFB uptake, with and without KClO<sub>4</sub>, between NIS-positive and control cells, as well as to compare AP parameters of RhiPSC-CMs obtained by patch clamp. In the event the assumptions of normality or equal variances were unsatisfied, the Wilcoxon signed-rank test was performed. A *P* value of  $<.05$  was selected to determine significance.

# 3 | RESULTS

## 3.1 | CRISPR/Cas9-engineered RhiPSCs demonstrate functional NIS expression

Following targeted knock-in of the rhesus *NIS* (*SLC5A5*) cDNA into the "safe harbor" AAVS1 locus via CRISPR/Cas9-mediated homologous recombination (Figure 1A and Figure S1), clones with high level *NIS* transgene expression were identified via immunostaining (Figure 1B) and used for all subsequent studies. NIS-RhiPSCs continued to form colonies that were morphologically indistinguishable from parental nontransgenic RhiPSCs and maintained normal karyotypes (Figure 1C). The functionality of the expressed *NIS* transporter was evaluated by cellular uptake of <sup>18</sup>F-TFB from culture media, with significantly greater uptake observed in NIS-RhiPSCs compared to NIS-negative control RhiPSCs ( $P = .0471$ , Figure 1D). <sup>18</sup>F-TFB uptake was attenuated to background levels in the presence of KClO<sub>4</sub>, an established *NIS* inhibitor,<sup>18</sup> indicating tracer uptake was specific and NIS-dependent ( $P = .0400$ ).

## 3.2 | NIS-RhiPSC-derived teratomas trackable in vivo

To demonstrate the utility of this platform for longitudinal in vivo imaging,  $5 \times 10^6$  NIS-RhiPSCs were injected subcutaneously into the hind limb of NSG mice and serially imaged for 6 weeks with PET/CT

(Figure 2A). NIS-RhiPSC-derived teratomas could be visualized on imaging as early as 2 weeks postinjection, 4 weeks prior to the development of a palpable mass, while NIS-negative RhiPSC-derived teratomas were not visible at any of the imaging time points. The size, morphology, and spatial distribution of NIS-positive teratomas could be followed longitudinally, and both tumor-to-muscle mean SUV ratios and total lesion  $^{18}\text{F}$ -TFB uptake of the tumors increased over the follow-up period in each replicate (Figure 2B). At 4 to 6 weeks, teratomas were harvested and subjected to histopathological analysis. NIS-RhiPSC-derived teratomas were indistinguishable from control RhiPSC-derived teratomas, exhibiting all three germ layers on histologic analysis (Figure S2). Persistent RhNIS expression was also demonstrated by immunohistochemical staining of NIS-RhiPSC-derived teratomas. Of note, some heterogeneity was observed in the level of

NIS expression between different cell types within the teratoma, although all cells expressed NIS above background. This finding was consistent with previously observed heterogeneity in expression of other marker genes knocked into the AAVS1 site in RhiPSCs.<sup>6</sup>

### 3.3 | NIS-RhiPSC-CMs retain functional NIS expression

NIS-RhiPSCs and parental control RhiPSCs underwent cardiac differentiation as previously described.<sup>12</sup> The overall kinetics and efficiency of cardiac differentiation of NIS-RhiPSCs were similar to that of parental RhiPSCs. NIS-RhiPSC-derived cardiomyocytes maintained characteristic cellular morphology, could be obtained with high purity,

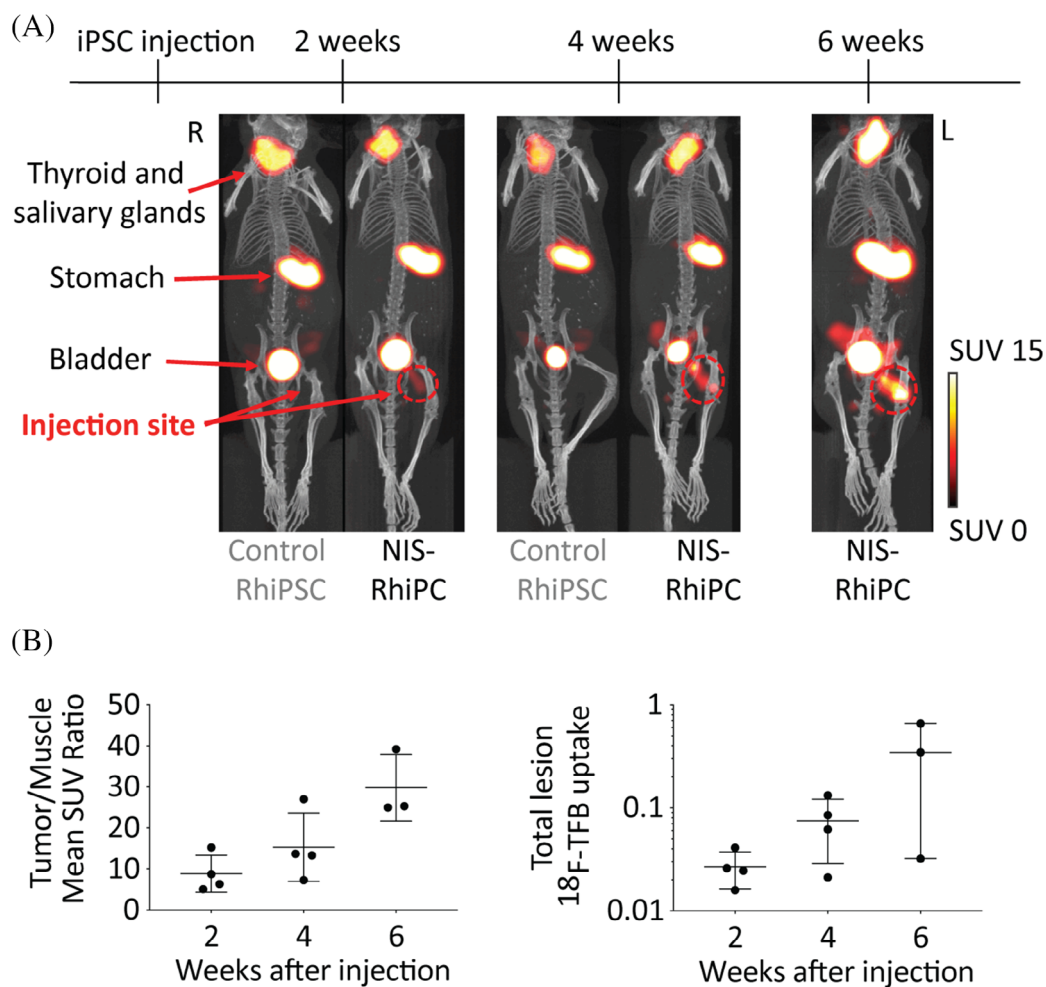


**FIGURE 2** NIS enables in vivo tracking of RhiPSC-derived teratomas. A, Delivery of RhNIS into RhiPSCs enables longitudinal in vivo tracking of NIS-RhiPSC-derived teratomas by PET/CT. After inoculating 5 million cells, NIS-RhiPSC-derived teratomas could be visualized as early as 2 weeks postinjection, and continued growth was observed at both 4 and 6 weeks.  $^{18}\text{F}$ -TFB signals were observed as expected in organs with known endogenous NIS expression, such as the thyroid, salivary glands, stomach, seminal vesicles, and also in the urinary bladder, indicating renal excretion of  $^{18}\text{F}$ -TFB. Two additional infero pelvic foci of  $^{18}\text{F}$ -TFB uptake were observed in male mice, possibly representing perianal glands. Maximal intensity projection images of PET merged with CT are shown. B, Tumor/muscle mean SUV ratios (left) and total lesion  $^{18}\text{F}$ -TFB uptake (right) increased over the follow-up period in all replicates ( $n = 4$ ), however one mouse underwent sacrifice at 4 weeks postinjection for histopathological examination. Error bars represent mean  $\pm$  SD.  $^{18}\text{F}$ -TFB,  $^{18}\text{F}$ -tetrafluoroborate; CT, computed tomography; PET, positron emission tomography; RhiPSCs, rhesus macaque induced pluripotent stem cells; SUV, standardized uptake value

and exhibited spontaneous beating in culture. NIS-RhiPSC-CMs manifested expected expression of canonical cardiac markers, including CTnT, NKX2.5, and  $\alpha$ -actinin (Figures and S3) at levels indistinguishable from cardiomyocytes differentiated from parental RhiPSCs. There were no apparent derangements in sarcomeric structures in NIS-positive vs NIS-negative RhiPSC-CMs, and ectopic NIS expression did not appear to alter the cardiogenic potential of RhiPSCs. No differentiation-induced NIS silencing was observed in any of the independent cardiomyocyte differentiation experiments ( $n = 5$ ; Figure 3A). Like undifferentiated NIS-RhiPSCs, NIS-RhiPSC-CMs demonstrated significantly greater  $^{18}\text{F}$ -TFB uptake than control RhiPSC-CMs ( $P = .0002$ ), with expected attenuation by  $\text{KClO}_4$ , a specific NIS inhibitor ( $P = .0042$ , Figure 3B).

To confirm that NIS-RhiPSC-CMs were detectable in vivo and assess sensitivity, we carried out intramuscular (IM) injections of various numbers of NIS-RhiPSC-CMs or control RhiPSC-CMs, followed by immediate  $^{18}\text{F}$ -TFB administration and PET/CT imaging 1 hour later ( $n = 3$ ). In each of the mice assessed, regions that underwent injections of control parental RhiPSC-CMs exhibited no detectable signal, while signals were reliably detected in sites where NIS-RhiPSC-CMs were introduced (Figure 3C). Of note, as few as  $1 \times 10^5$  NIS-RhiPSC-CMs could be detected in vivo following local IM injection (Figure S4).

### 3.4 | EP characterization of NIS-RhiPSC-CMs

To investigate the impact of NIS expression upon EP parameters of NIS-RhiPSC-CMs, a combination of whole-cell patch clamp and optical imaging was used. At day 20 to 25 of differentiation, patch clamp recording documented the presence of nodal-, atrial-, and ventricular-like cardiomyocytes by established AP morphological features, and there were no gross perturbations in baseline AP morphology in NIS-RhiPSC-CMs compared to parental control RhiPSC-CMs (Figure 4A, upper panel). Consistent with prior studies on both human and rhesus iPSC-CMs,<sup>12,19</sup> ventricular-type CMs constituted the majority of the cells after differentiation (Figure 4B). NIS expression in RhiPSC-CMs did not induce significant deviations in most AP parameters such as baseline resting potential, AP amplitude, or AP duration at 90% repolarization ( $\text{APD}_{90}$ ) when compared with controls across all CM subtypes. Of note,  $V_{\text{max}}$  was found to be significantly higher in NIS-positive atrial-like cells ( $23.30 \pm 3.91$  vs  $9.92 \pm 0.73$  [V/s];  $P = .0405$ ) compared to control atrial-like cells; however, this trend was not observed among nodal- or ventricular-type CMs. Overall, each of the aforementioned EP indices was comparable to previously reported ranges for human and NHP PSC-CMs at similar stages of development.<sup>12,20-23</sup> Finally, simultaneous recording of calcium ( $\text{Ca}^{2+}$ ) flux revealed well-coupled  $\text{Ca}^{2+}$  transients to their respective APs in each of the cardiomyocyte subtypes (Figure 4A, lower panel).

Although there is evidence to suggest that NIS participates in sodium flux in an anion-independent manner, and thus might

influence EP characteristics even at baseline, NIS current has been shown to be largely anion-dependent.<sup>24</sup> Hence, we next assessed the impact of iodide on EP parameters in NIS-positive and control CMs. Iodide was selected to maximize the sensitivity of these and subsequent studies, as it has been demonstrated to yield higher NIS-dependent transmembrane potentials than TFB or other NIS-transported anions.<sup>24</sup> Preliminary data were gathered by whole-cell patch clamp, in which ventricular-like NIS-RhiPSC-CMs ( $n = 5$ ) were exposed to 1 mM NaI, more than 3000-fold greater than the upper limit of the normal serum level of free iodide.<sup>24-26</sup> Even at these levels of NaI, there were no appreciable derangements in overall spontaneous AP morphology or in each of the measured EP parameters vs pre-exposure baseline (Figure 5A-D). To determine whether the presence of NaI altered  $\text{Ca}^{2+}$  handling, beating single NIS-RhiPSC-CMs ( $n = 3$ ) were again exposed to the  $\text{Ca}^{2+}$  indicator Cal-520. Peak fluorescence amplitude, as well as the rate of fluorescence decline ( $\text{CaD}_{50}$ ), were similar in the presence and absence of 1 mM NaI, indicating that NaI did not exert a significant effect on intracellular  $\text{Ca}^{2+}$  levels or on overall  $\text{Ca}^{2+}$  handling compared to baseline (Figure 5E-G).

As only small numbers of individual cells can be assessed using patch clamp approaches, we also used high-throughput optical imaging with voltage-sensitive dyes (VSD) to further investigate EP differences between control and NIS-positive RhiPSC-CMs. These techniques permit evaluation of EP parameters in much larger populations of cells, and have previously enabled detection of action potential duration (APD) prolongation in iPSC-CMs after administration of drugs known to induce clinical QT prolongation,<sup>27</sup> a significant risk factor for lethal ventricular arrhythmias. Hence, we elected to focus on  $\text{APD}_{90}$  for these studies. The VSD analyses were carried out under escalating NaI concentrations, and APs were obtained both at baseline and after treatment. To control for variation in spontaneous beating rate between wells,  $\text{APD}_{90}$  measurements were normalized to the observed rate in each well ( $\text{APD}_{90\text{C}}$ ), then corrected for vehicle-induced change from baseline ( $\Delta\Delta\text{APD}_{90\text{C}}$ ). Consistent with the results obtained by patch clamp, no perturbations in  $\Delta\Delta\text{APD}_{90\text{C}}$  were observed between NIS-RhiPSC-CMs and control at baseline ( $P = .61$ ), nor were any significant differences in NIS-RhiPSC-CMs relative to baseline at 10  $\mu\text{M}$  NaI, approximately 30-fold the physiologic serum level of free iodide. However, after 45-minute treatment with 100  $\mu\text{M}$  NaI, a concentration 300-fold higher than physiologic levels, we observed a significant increase in  $\Delta\Delta\text{APD}_{90\text{C}}$  in NIS-RhiPSC-CMs relative to baseline ( $P < .01$ ; Figure 5H). This finding was also noted following incubation with 1000  $\mu\text{M}$  NaI ( $P < .01$ ; Figure 5H); however, the magnitude of these deviations was small at both of these supraphysiologic concentrations, on average 17% and 24% of baseline for each of the aforementioned NaI levels, respectively. Notably, no significant change in  $\Delta\Delta\text{APD}_{90\text{C}}$  was seen in control RhiPSC-CMs at any level of NaI compared to baseline (Figure 5H, left panel). Additionally, forms of triggered activity, such as early or delayed after depolarizations, were not observed at any of the NaI levels assessed. Taken together, these results indicate that NIS does not significantly impact

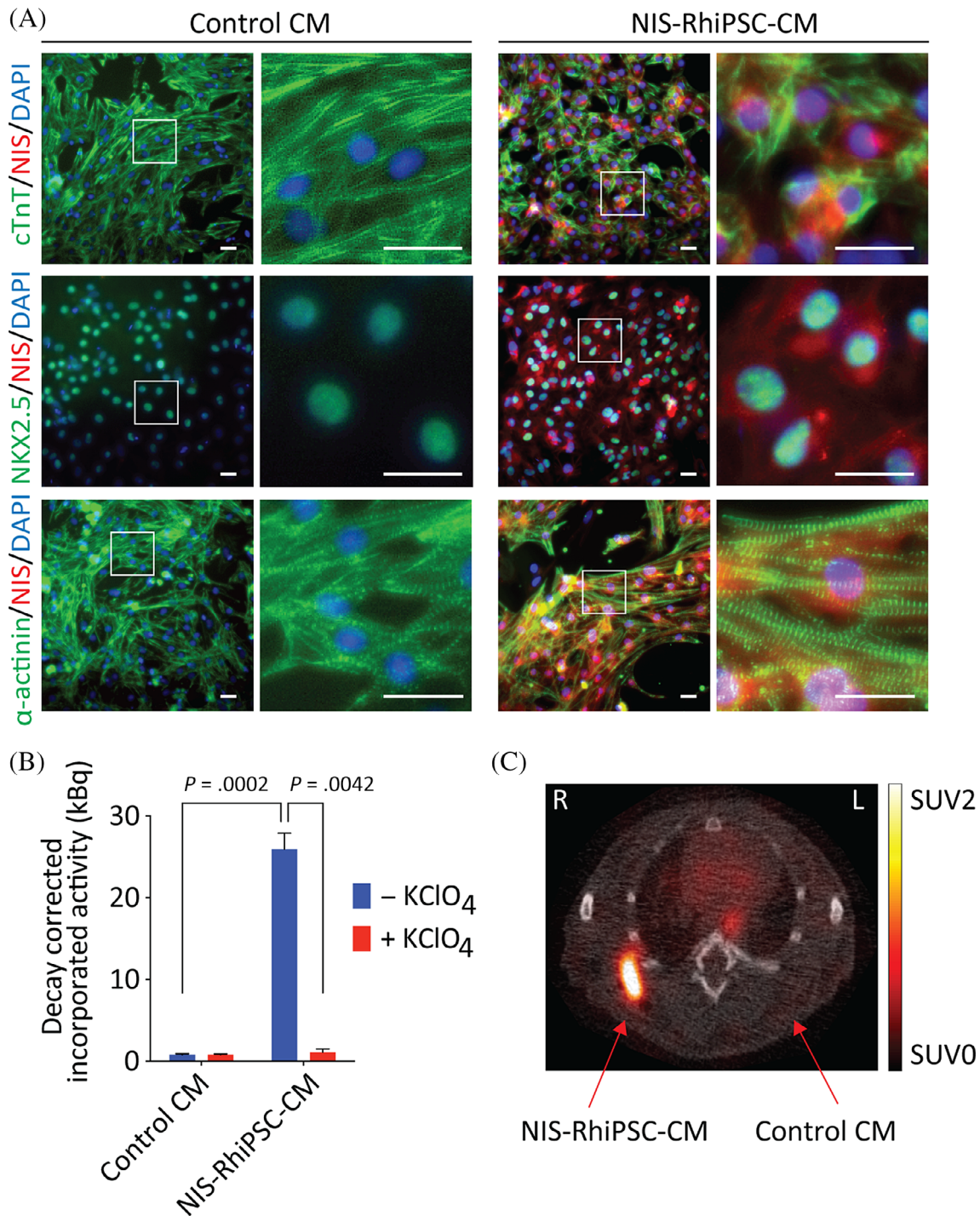


**FIGURE 3** NIS-RhiPSC-CMs retain functional NIS expression. A, Immunostaining at day 20 of cardiac differentiation shows phenotypically normal RhiPSC-CMs with preserved NIS expression (red in all panels). NIS-RhiPSC-CMs exhibit characteristic staining patterns for CTnT (first row, green), NKX2.5 (second row, green), and  $\alpha$ -actinin (third row, green). Per CTnT and  $\alpha$ -actinin costaining, there were no detectable derangements in sarcomeric structures. All replicates were counterstained with DAPI (blue). Scale bar = 50  $\mu$ m. B, NIS-RhiPSC-CMs retained expression of functional RhNIS per <sup>18</sup>F-TFB uptake assay. NIS-RhiPSC-CMs exhibited significantly greater uptake of <sup>18</sup>F-TFB vs control RhiPSC-CMs (n = 3). Tracer uptake was again ablated in the presence of KClO<sub>4</sub>, confirming NIS-dependence. Error bars represent mean  $\pm$  SEM. C, Intramuscular injection of 2 million NIS-RhiPSC-CMs and control (NIS-negative) RhiPSC-CMs with subsequent <sup>18</sup>F-TFB intravenous injection and imaging via PET/CT 1 hour later (n = 3). Transverse slices through NIS-RhiPSC-CM injection sites at upper limb show readily visible cell-derived signals. No detectable signal was observed following injection of control RhiPSC-CMs. <sup>18</sup>F-TFB, <sup>18</sup>F-tetrafluoroborate; CT, computed tomography; DAPI, 4',6-diamidino-2'-phenylindole dihydrochloride; PET, positron emission tomography; RhiPSC-CMs, rhesus macaque induced pluripotent stem cell-derived cardiomyocytes



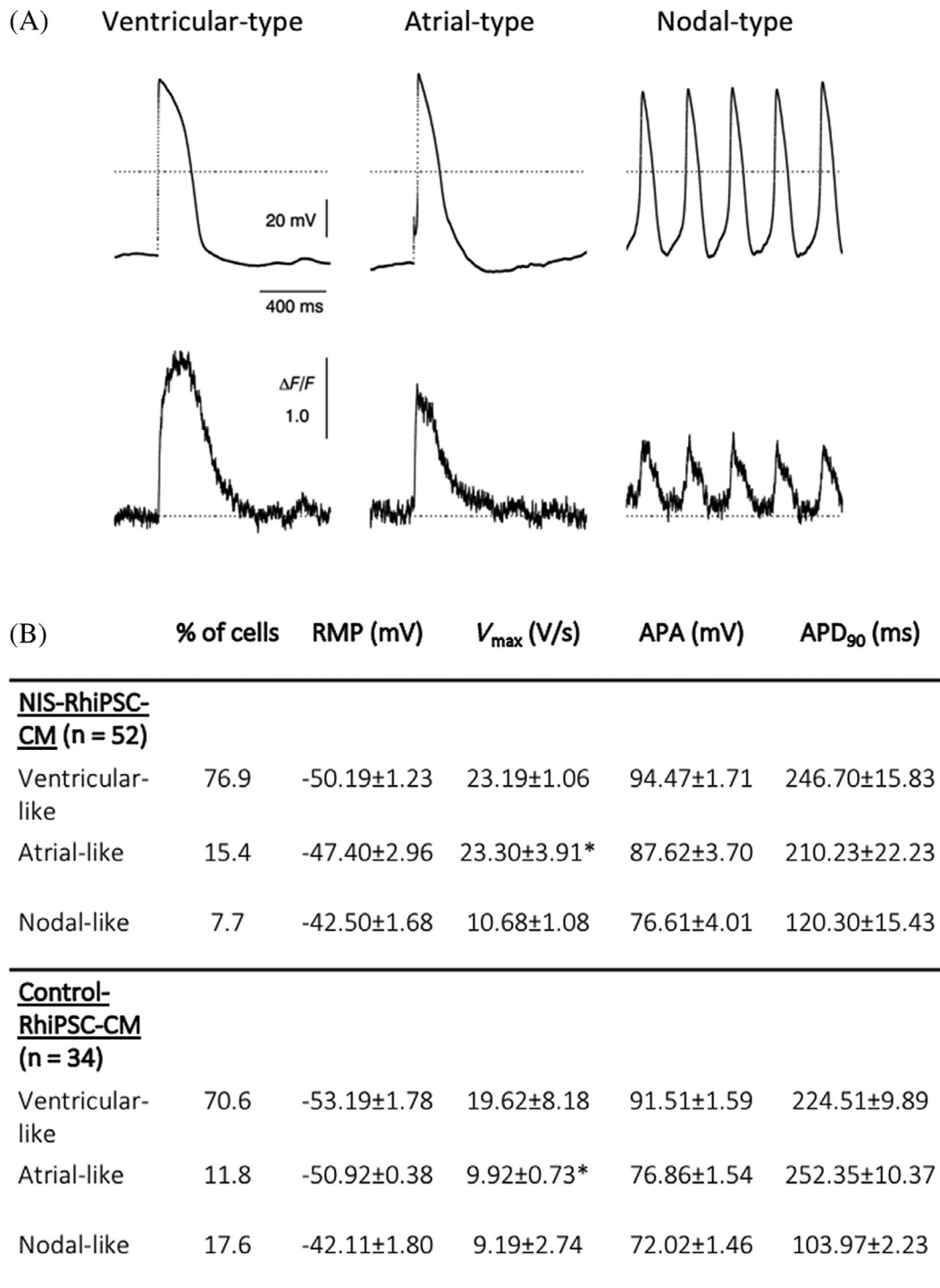


**FIGURE 4** Electrophysiological characteristics of NIS-RhiPSC-CMs. A, Coupling of action potential (top) and  $\text{Ca}^{2+}$  flux (bottom), shown via simultaneous recording by patch clamp and  $\text{Ca}^{2+}$  fluorescence imaging of three different cardiomyocyte subtypes derived from NIS-RhiPSCs. B, Baseline electrophysiological parameters of NIS-RhiPSC-CMs and control RhiPSC-CMs by whole-cell patch clamp in each of the CM subtypes, expressed as mean  $\pm$  SEM. Statistical analysis between NIS-RhiPSC-CMs and control RhiPSC-CMs was performed with a *t* test for independent samples. \**P* < .05. RhiPSC-CMs, rhesus macaque induced pluripotent stem cell-derived cardiomyocytes

EP parameters of RhiPSC-CMs at baseline, nor at iodide levels up to 30-fold higher than normal serum levels. However, when exposed to massively supraphysiologic levels of NaI, NIS-positive CMs exhibited a small dose-dependent increase in  $\Delta\Delta\text{APD}_{90\text{C}}$ , suggestive of an effect of NIS-dependent ion transport.

### 3.5 | Longitudinal in vivo tracking of transplanted NIS-RhiPSC-CMs via PET/CT

Myocardial infarction was induced in immunodeficient mice by 90-minute ligation of the LAD followed by reperfusion. Immediately

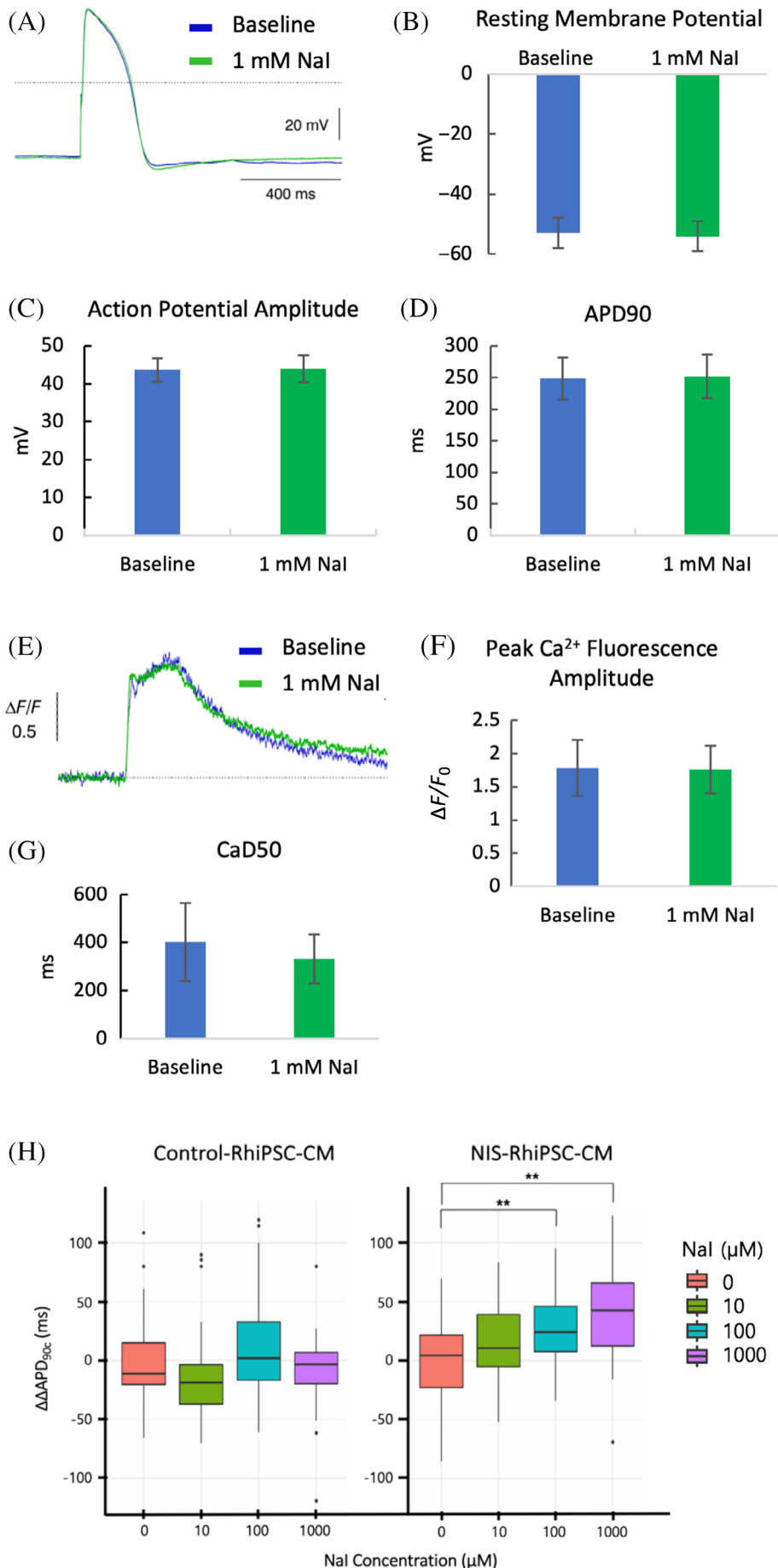


**FIGURE 5** Electrophysiological (EP) characteristics of NIS-RhiPSC-CMs after addition of sodium iodide (NaI). A, Representative AP tracings at pre-exposure baseline (blue) and 3 minutes after addition of 1 mM NaI (green) in V-type NIS-RhiPSC-CMs (n = 5). Images obtained via whole-cell patch clamp. B-D, Graphic representation of key EP parameters in NIS-RhiPSC-CMs, both before and during incubation with 1 mM NaI (n = 5), expressed as mean ± SEM. E, Representative Ca<sup>2+</sup> transients at pre-exposure baseline (blue) and 3 minutes after addition of 1 mM NaI (green) in V-type NIS-RhiPSC-CMs (n = 3). F, G, Graphic representation of peak Ca<sup>2+</sup> fluorescence and time to 50% Ca<sup>2+</sup> fluorescence decay (CaD<sub>50</sub>) in NIS-RhiPSC-CMs, both before and during incubation with 1 mM NaI (n = 3), expressed as mean ± SEM. H, Optical imaging with voltage-sensitive dyes revealed a progressive increase in ΔΔAPD<sub>90c</sub> in NIS-RhiPSC-CMs (n = 96) relative to baseline with escalating levels of NaI, becoming significant at 100 μM NaI and remaining significant at 1000 μM NaI. No significant deviations were observed in control RhiPSC-CMs (n = 107) at any of the NaI levels assessed. Data are represented as box plots, wherein the middle line, box ends, and whiskers represent the median, first and third quartiles, and minimum and maximum values, respectively. Dots on either side of the whiskers are outliers. \*\*P < .01. AP, action potential; RhiPSC-CMs, rhesus macaque induced pluripotent stem cell-derived cardiomyocytes



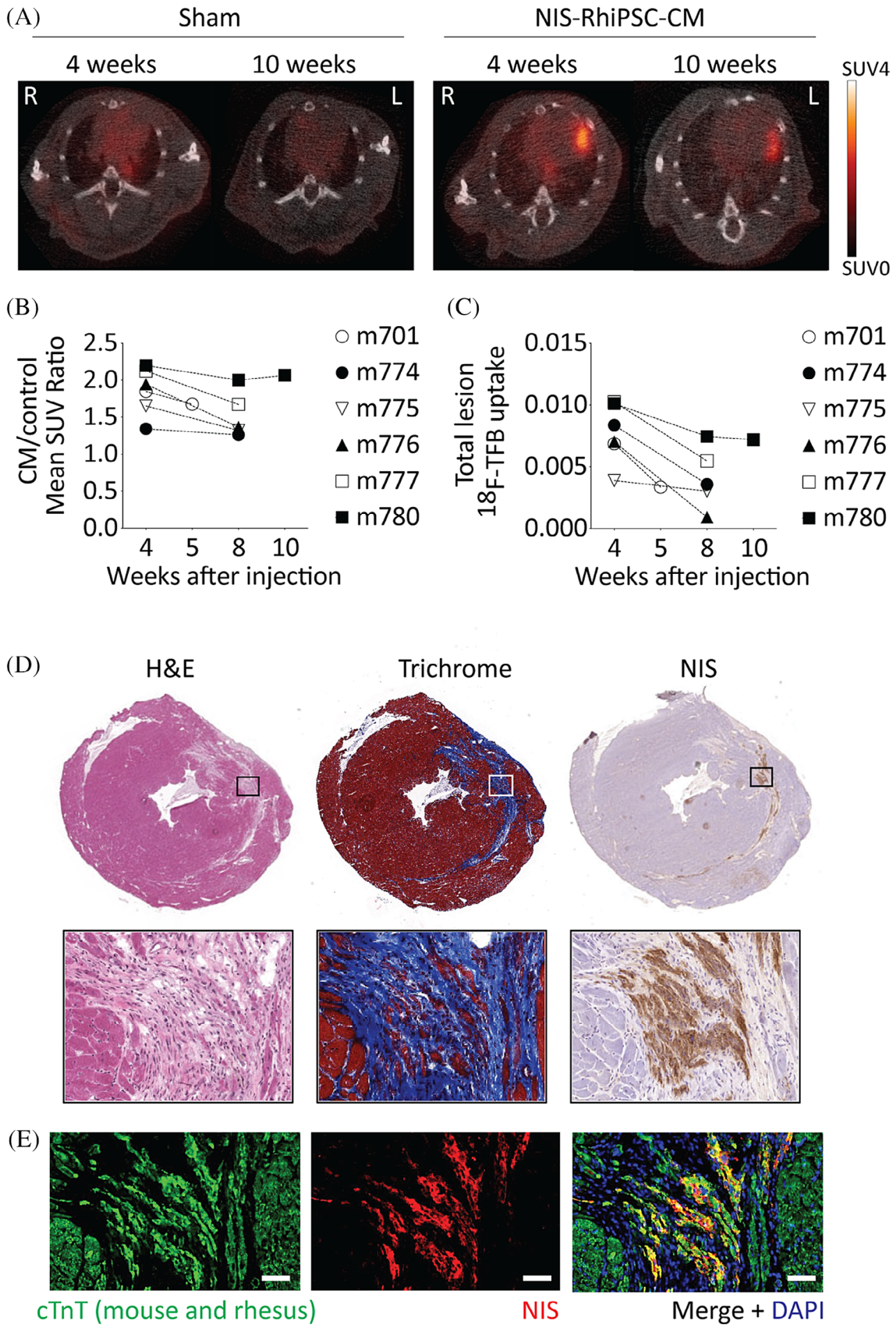


**FIGURE 6** Legend on next page.

following reperfusion,  $2 \times 10^6$  NIS-RhiPSC-CMs ( $n = 10$ ) or vehicle alone ( $n = 4$ ) were injected into the infarct zone. For in vivo imaging of the injected hearts, serial  $\mu$ PET/CT was performed every 1 to 4 weeks. Table S1 summarizes the results. No signals were visualized after injection of vehicle alone. In the cohort that underwent cell injection, transplanted cells were clearly and quantifiably visualized via PET/CT in six out of 10 animals during the follow-up period (Figures 6A-C and S5 Video S1).

In the PET-positive animals, intracardiac signals were putatively derived from engrafted NIS-positive CMs within the left ventricular myocardium. This was confirmed via microscopic analysis of the explanted hearts, with NIS+/CTnT+ double-positive cells observed throughout the LAD-territory scar (Figure 6D,E). Virtually all NIS+ cells were also positive for CTnT, and there was no evidence for teratoma formation. In addition, NIS expression appeared homogenous across the cardiomyocytes within the infarct scars, implying no loss of NIS expression over time in maturing and engrafted cardiomyocytes. Hearts from one of the four mice in the cell-injection cohort that failed to exhibit a detectable PET signal (PET-negative) also underwent histopathological examination, revealing minimal engraftment of NIS+ cells relative to its PET-positive counterparts (Figure S6 Table S1).

Tissues from the remaining three PET-negative mice did not undergo further histopathological analysis. No teratomas or other undifferentiated cells were observed in the tissue sections, and no ectopic PET signals consistent with extra-cardiac tumor formation were observed throughout the follow-up period.

## 4 | DISCUSSION

Molecular imaging techniques that enable long-term tracking of cells after myocardial delivery are crucial for optimizing the safety and therapeutic efficacy of cardiac cellular therapies. NIS is a non-immunogenic endogenous gene that can be repurposed to monitor persistence and localization of cellular therapies via standard clinical imaging modalities. In the current study, we demonstrate for the first time that CRISPR/Cas9-mediated introduction of the NIS reporter gene enables stable longitudinal imaging of iPSC-CMs after engraftment into infarcted myocardium, and permits sensitive detection of teratomas developing from undifferentiated engrafted iPSCs.

We have previously shown that marker transgenes such as green fluorescent protein (GFP) and human truncated CD19 can be robustly

and stably expressed following CRISPR/Cas9-mediated targeted introduction at the AAVS1 safe harbor locus, a site in the genome permitting high level constitutive expression without genotoxicity.<sup>6</sup> However, neither of these transgenes is suitable for high-resolution longitudinal in vivo imaging, thus we used the CRISPR/Cas9 genome editing system to introduce the NIS transgene into the AAVS1 site. Expression of NIS was sufficiently robust and stable to allow sensitive and specific noninvasive imaging of engrafted cells in live animals via PET/CT. In contrast to lentiviral transduction, which may result in multiple copies per cell, CRISPR/Cas9 targeted transgene introduction into the AAVS1 locus results in only one, or at most two, copies per cell. Despite this limited copy number per cell, our methodology resulted in an in vivo threshold of detection of as few as  $1 \times 10^5$  injected cells—on par with prior studies using lentiviral vectors for NIS integration.<sup>4,5</sup> Use of CRISPR/Cas9 AAVS safe harbor targeting also overcomes two potential drawbacks of using lentiviral vectors to deliver NIS, specifically genotoxicity related to semi-random genome integration and developmental silencing of lentiviral vector-encoded transgenes.<sup>28-31</sup>

In the present study, NIS expression did not appear to affect differentiation capacity of iPSCs into all three germ layers in NIS-iPSC-derived teratomas. Furthermore, consistent with a prior study using rat cardiac-derived stem cells,<sup>5</sup> there were no changes in the efficiency of cardiomyocyte differentiation from NIS-iPSCs. This is important as delivery of large numbers of cells, at least  $10^8$  to  $10^9$ , are likely required to facilitate cardiac regeneration in humans based on large-animal data,<sup>32-34</sup> and any reduction in differentiation efficiency could impose significant feasibility constraints upon large-scale cell production protocols. Differentiation-induced NIS silencing was not observed. NIS-RhiPSC-CMs exhibited intact expression of key cardiomyocyte markers and structural features, and successfully engrafted in infarcted myocardium after local injection. Most importantly, despite small infarct sizes, NIS-positive iPSC-CMs could be detected and localized in the heart for up to 10 weeks postinjection via PET/CT.

Prior investigation has demonstrated that adenoviral transfection of NIS into rat hearts does not result in significant myocardial injury or dysfunction relative to a control GFP-carrying vector,<sup>35</sup> However, although NIS is known to be electrogenic,<sup>24</sup> the impact of ectopic NIS expression on EP parameters in cardiomyocytes has not been thoroughly assessed. This is an important step as any derangement in impulse conduction might predispose to lethal arrhythmia formation in more advanced in vivo models, or even clinical trials. Overall,

**FIGURE 6** Longitudinal in vivo tracking of NIS-RhiPSC-CMs by  $\mu$ PET/CT. A, Intramyocardial signals within the putative infarct zone can be readily visualized at both 4 and 10 weeks in the NIS-RhiPSC-CM injection animal (right) vs the sham vehicle injection animal (left). Representative PET/CT images are shown. Display settings shared by all images. B,C, Quantification  $^{18}$ F signals of implanted NIS-RhiPSC-CMs in PET-positive animals over time. D, Histologic analysis of explanted PET-positive hearts revealed small left anterior descending artery-territory infarcts by H&E (left), shown more clearly by trichrome staining (middle). Immunostaining for NIS highlights engraftment of NIS+ cells throughout the infarct region (right) in this representative image. Images in top and bottom panels obtained at 40X and 320X, respectively. E, Costaining of NIS (red) and CTnT (green) confirmed engraftment of NIS-RhiPSC-CMs in infarct zone. CTnT is expressed in both mouse and rhesus cardiomyocytes. All images in (D, E) were obtained from the same injected mouse shown in panel (A), right. Scale bar = 50  $\mu$ m.  $\mu$ PET, micro-positron emission tomography; CT, computed tomography; RhiPSC-CMs, rhesus macaque induced pluripotent stem cell-derived cardiomyocytes

characteristic AP parameters between NIS-positive and control CMs at baseline were very similar, particularly for ventricular and nodal type cells, and within reported normal ranges. As NIS current is anion-dependent,<sup>24</sup> we then examined key EP features in the presence of iodide. By patch clamp, we did not observe any notable derangements in overall AP morphology, or in any of the EP parameters assessed for ventricular cardiomyocytes with Nal exposure. However, the cell numbers in the patch clamp studies were limited, and AP tracings were obtained shortly following Nal administration. By subjecting control and NIS-positive CMs to high-throughput optical imaging with VSD, a progressive prolongation of the  $\Delta\Delta\text{APD}_{90\text{C}}$  in NIS-RhiPSC-CMs with increasing amounts of Nal was revealed, becoming significant at 100  $\mu\text{M}$  Nal. Of note however, this level of iodide represents greater than 300-fold the reported normal serum level of free iodide.<sup>24-26</sup> As it was not evident in control CMs, this finding possibly reflects increased iodide-driven inward  $\text{Na}^+$  current via NIS, leading to a protracted repolarization phase. However, additional studies are needed to clarify the precise mechanism of the observed  $\text{APD}_{90}$  prolongation in NIS-RhiPSC-CMs. It must be noted that the effect size of the observed  $\text{APD}_{90\text{C}}$  prolongation was small, hence while the increase in  $\Delta\Delta\text{APD}_{90\text{C}}$  at these levels of Nal was significant, it was substantially lower than has been observed in other *in vitro* iPSC-CM models of drug-induced or genetically induced QT prolongation.<sup>27,36,37</sup> In addition, we did not observe other key findings reported in channelopathic iPSC-CM lines, such as  $\text{Ca}^{2+}$ -transient irregularities and early after depolarizations,<sup>36,38</sup> even in the presence of massively supraphysiologic Nal. Taken together, this data indicate that ectopic expression of NIS is not likely to significantly impact the EP parameters of iPSC-CMs under *in vivo* conditions.

Last, a principal utility of NIS-based imaging platforms lies in their translatability. NIS is compatible with a wide range of safe and effective molecular imaging modalities and radiotracers, including several already used in the clinic, such as  $^{124}\text{I}$  and  $^{99\text{m}}\text{Tc}$  pertechnetate ( $^{99\text{m}}\text{TcO}_4^-$ ). Here, we elected to pursue PET imaging with  $^{18}\text{F}$ -TFB based on overall superior sensitivity and appreciably shorter half-life (110 minutes) compared to other NIS-compatible radiotracers.<sup>39</sup> In addition to enabling more frequent imaging, this short half-life minimizes radiation exposure to both the patient and graft. Notably, prior studies have shown that the interaction between NIS and TFB is significantly less electrogenic than with iodide-based preparations. Hence, as our data indicate significant iodide loads can provoke dose-dependent APD prolongation,  $^{18}\text{F}$ -TFB is a conceivably safer option in imaging platforms using NIS. However, while it must be noted that  $^{18}\text{F}$ -TFB is not yet FDA approved for molecular imaging, it has been safely used in recent clinical studies,<sup>40,41</sup> and other NIS-compatible radiotracers can be used while awaiting approval.

Several limitations must be acknowledged. First, only imaging outcomes after cell transplantation were robustly assessed in this study, hence we are unable to evaluate the functional impact of NIS-iPSC-CMs on the infarcted hearts. However, multiple prior investigations in large animals have demonstrated the ability of PSC-CMs to impart structural or functional improvement after transplantation into infarcted hearts.<sup>32-34</sup> Additionally, although the findings in this study

indicate that NIS is not likely to significantly impact EP parameters in iPSC-CMs under physiologic conditions, their application in large animal studies is required for definitive assessment of both baseline and iodide-evoked arrhythmogenicity. To facilitate clinical translation by showing viability in platform compatible with downstream NHP models, this study used RhiPSC-CMs. Although RhiPSC-CMs and hiPSC-CMs are phenotypically and functionally similar, including comparable reference ranges for EP characteristics, further investigation is necessary to investigate the impact of NIS expression in hiPSC-CMs before application in future clinical cardiomyocyte cell therapy trials.

## 5 | CONCLUSION

In this study, site-specific expression of the sodium-iodide symporter via the AAVS1 safe harbor locus was shown to enable sensitive, longitudinal, and readily quantifiable *in vivo* tracking of iPSC-CMs in a clinically relevant model of myocardial infarction, without provocation of significant differences in EP parameters when compared with control. This approach holds significant promise for application in downstream clinical and preclinical trials of cardiac cell therapies.

### ACKNOWLEDGMENTS

We are grateful to Stefan Cordes for his generous advice and help with statistical analyses. We thank Shiqin Judy Yu for assisting with iPSC culture. We also thank NHLBI core facilities, including the Animal Surgery and Resources Core for surgical support, the Pathology Core for tissue processing, and the Light Microscopy Core for imaging analyses, as well as the NCI Clinical Research Center Animal Facility staff for provision of excellent animal care. This research was supported by funding from the Division of Intramural Research program of the NHLBI and NCI. J. W. O. was supported by the Medical Research Scholars Program of the NIH.

### CONFLICT OF INTEREST

K.-W.P. is a cofounder, co-owner, and holds equity in Imanis Life Sciences. Imanis Life Sciences has not funded any aspect of this research. The other authors declared no potential conflicts of interest.

### AUTHOR CONTRIBUTIONS

J.W.O., R.Y.: collection and assembly of data, data analysis and interpretation, manuscript writing; N.S., M.K., K.B., D.P., R.V., M.P., H.S., Y.L., F.B., X.Z., R.E.S.: collection and assembly of data, data analysis and interpretation; S.P., K.-W.P., M.H., P.L.C., J.Z.: data analysis and interpretation; M.B.: data analysis and interpretation, financial support; S.H.: conception and design, collection and assembly of data, data analysis and interpretation, manuscript writing; C.E.D.: conception and design, data interpretation, manuscript writing, financial support.

### DATA AVAILABILITY STATEMENT

The data that support the findings of this study are available from corresponding authors upon request.



## ORCID

So Gun Hong  <https://orcid.org/0000-0002-3538-5444>Cynthia E. Dunbar  <https://orcid.org/0000-0002-7645-838X>

## REFERENCES

- Chen IY, Wu JC. Cardiovascular molecular imaging: focus on clinical translation. *Circulation*. 2011;123(4):425-443.
- Ravera S, Reyna-Neyra A, Farrandino G, et al. The sodium/iodide symporter (NIS): molecular physiology and preclinical and clinical applications. *Annu Rev Physiol*. 2017;79:261-289.
- Lee AR, Woo SK, Kang SK, et al. Adenovirus-mediated expression of human sodium-iodide symporter gene permits in vivo tracking of adipose tissue-derived stem cells in a canine myocardial infarction model. *Nucl Med Biol*. 2015;42:621-629.
- Templin C, Zweigerdt R, Schwanke K, et al. Transplantation and tracking of human-induced pluripotent stem cells in a pig model of myocardial infarction: assessment of cell survival, engraftment, and distribution by hybrid single photon emission computed tomography/computed tomography of sodium iodide symporter transgene expression. *Circulation*. 2012;126(4):430-439.
- Terrovitis J, Kwok KF, Lautamaki R, et al. Ectopic expression of the sodium-iodide symporter enables imaging of transplanted cardiac stem cells in vivo by single-photon emission computed tomography or positron emission tomography. *J Am Coll Cardiol*. 2008;52(20):1652-1660.
- Hong S, Yada RC, Choi K, et al. Rhesus iPSC safe harbor gene-editing platform for stable expression of transgenes in differentiated cells of all germ layers. *Mol Ther*. 2017;25(1):44-53.
- Papapetrou EP, Schambach A. Gene insertion into genomic safe harbors for human gene therapy. *Mol Ther*. 2016;24(4):678-684.
- Liu H, Zhu F, Yong J, et al. Generation of induced pluripotent stem cells from adult rhesus monkey fibroblasts. *Cell Stem Cell*. 2008;3(6):587-590.
- Hong S, Winkler T, Wu C, et al. Path to the clinic: assessment of iPSC-based cell therapies in vivo in a nonhuman primate model. *Cell Rep*. 2014;7(4):1298-1309.
- Zhao X, Chen H, Xiao D, et al. Comparison of non-human primate versus human induced pluripotent stem cell-derived cardiomyocytes for treatment of myocardial infarction. *Stem Cell Reports*. 2018;10(2):422-435.
- Yada RC, Hong S, Lin Y, et al. Rhesus macaque iPSC generation and maintenance. *Curr Protoc Stem Cell Biol*. 2017;41:4A.11.1-4A.11.13.
- Lin Y, Liu H, Klein M, et al. Efficient differentiation of cardiomyocytes and generation of calcium-sensor reporter lines from nonhuman primate iPSCs. *Sci Rep*. 2018;8(1):5907.
- Yada RC, Ostrominski JW, Tunc I, et al. CRISPR/Cas9-based safe-harbor gene editing in rhesus iPSCs. *Curr Protoc Stem Cell Biol*. 2017;43:5A.11.1-5A.11.14.
- Hortigon-Vinagre MP, Zamora V, Burton FL, Green J, Gintant GA, Smith GL. The use of ratiometric fluorescence measurements of the voltage sensitive dye Di-4-ANEPPS to examine action potential characteristics and drug effects on human induced pluripotent stem cell-derived cardiomyocytes. *Toxicol Sci*. 2016;154(2):320-331.
- Jiang H, Bansal A, Pandey MK, et al. Synthesis of <sup>18</sup>F-tetrafluoroborate via radiofluorination of boron trifluoride and evaluation in a murine C6-glioma tumor model. *J Nucl Med*. 2016;57(9):1454-1459.
- Lee SB, Lee HW, Lee H, et al. Tracking dendritic cell migration into lymph nodes by using a novel PET probe (18F)-tetrafluoroborate for sodium/iodide symporter. *EJNMMI Res*. 2017;7(1):32.
- Samnick S, Al-Momani E, Schmid JS, et al. Initial clinical investigation of [18F]Tetrafluoroborate PET/CT in comparison to [124I]Iodine PET/CT for imaging thyroid cancer. *Clin Nucl Med*. 2018;43(3):162-167.
- Dingli D, Peng KW, Harvey ME, et al. Image-guided radiotherapy for multiple myeloma using a recombinant measles virus expressing the thyroidal sodium iodide symporter. *Blood*. 2004;103(5):1641-1646.
- Sanchez-Freire V, Lee AS, Hu S, et al. Effect of human donor cell source on differentiation and function of cardiac induced pluripotent stem cells. *J Am Coll Cardiol*. 2014;64(5):436-448.
- Burrige PW, Matsa E, Shukla P, et al. Chemically defined generation of human cardiomyocytes. *Nat Methods*. 2014;11(8):855-860.
- Robertson C, Tran DD, George SC. Concise review: maturation phases of human pluripotent stem cell-derived cardiomyocytes. *STEM CELLS*. 2013;31(5):829-837.
- Zhang J, Klos M, Wilson GF, et al. Extracellular matrix promotes highly efficient cardiac differentiation of human pluripotent stem cells: the matrix sandwich method. *Circ Res*. 2012;111(9):1125-1136.
- Sayed N, Liu C, Wu JC. Translation of human-induced pluripotent stem cells: from clinical trial in a dish to precision medicine. *J Am Coll Cardiol*. 2016;67(18):2161-2176.
- Eskandari S, Loo DD, Dai G, et al. Thyroid Na<sup>+</sup>/I<sup>-</sup>symporter. Mechanism, stoichiometry, and specificity. *J Biol Chem*. 1997;272(43):27230-27238.
- Carrasco N. Iodide transport in the thyroid gland. *Biochim Biophys Acta*. 1993;1154(1):65-82.
- Michalke B, Schramel P, Hasse S. Separation of free iodide from other I-species in human serum - quantification in serum pools and individual samples. *Anal Bioanal Chem*. 1996;354(5-6):576-579.
- Blinova K, Stohlman J, Vicente J, et al. Comprehensive translational assessment of human-induced pluripotent stem cell derived cardiomyocytes for evaluating drug-induced arrhythmias. *Toxicol Sci*. 2017;155(1):234-247.
- Cesana D, Ranzani M, Volpin M, et al. Uncovering and dissecting the genotoxicity of self-inactivating lentiviral vectors in vivo. *Mol Ther*. 2014;22(4):774-785.
- Herbst F, Ball CR, Tuorto F, et al. Extensive methylation of promoter sequences silences lentiviral transgene expression during stem cell differentiation in vivo. *Mol Ther*. 2012;20(5):1014-1021.
- Sadelain M, Papapetrou EP, Bushman FD. Safe harbours for the integration of new DNA in the human genome. *Nat Rev Cancer*. 2011;12(1):51-58.
- Wu C, Hong SG, Winkler T, et al. Development of an inducible caspase-9 safety switch for pluripotent stem cell-based therapies. *Mol Ther Methods Clin Dev*. 2014;1:14053.
- Chong JJ, Yang X, Don CW, et al. Human embryonic-stem-cell-derived cardiomyocytes regenerate non-human primate hearts. *Nature*. 2014;510(7504):273-277.
- Liu YW, Chen B, Yang X, et al. Human embryonic stem cell-derived cardiomyocytes restore function in infarcted hearts of non-human primates. *Nat Biotechnol*. 2018;36(7):597-605.
- Shiba Y, Gombuchi T, Seto T, et al. Allogeneic transplantation of iPSC cell-derived cardiomyocytes regenerates primate hearts. *Nature*. 2016;538(7625):388-391.
- Lee KH, Bae JS, Lee SC, et al. Evidence that myocardial Na/I symporter gene imaging does not perturb cardiac function. *J Nucl Med*. 2006;47(11):1851-1857.
- Itzhaki I, Maizels L, Huber I, et al. Modelling the long QT syndrome with induced pluripotent stem cells. *Nature*. 2011;471(7337):225-229.
- Moretti A, Bellin M, Welling A, et al. Patient-specific induced pluripotent stem-cell models for long-QT syndrome. *N Engl J Med*. 2010;363(15):1397-1409.
- Maizels L, Huber I, Arbel G, et al. Patient-specific drug screening using a human induced pluripotent stem cell model of catecholaminergic

- polymorphic ventricular tachycardia type 2. *Circ Arrhythm Electro-physiol.* 2017;10(6):e004725.
39. Jauregui-Osoro M, Sunassee K, Weeks AJ, et al. Synthesis and biological evaluation of [(18)F]tetrafluoroborate: a PET imaging agent for thyroid disease and reporter gene imaging of the sodium/iodide symporter. *Eur J Nucl Med Mol Imaging.* 2010;37(11):2108-2116.
  40. Jiang H, Schmit NR, Koenen AR, et al. Safety, pharmacokinetics, metabolism and radiation dosimetry of (18)F-tetrafluoroborate ((18)F-TFB) in healthy human subjects. *EJNMMI Res.* 2017;7(1):90.
  41. O'Doherty J, Jauregui-Osoro M, Brothwood T, et al. (18)F-tetrafluoroborate, a PET probe for imaging sodium/iodide symporter expression: whole-body biodistribution, safety, and radiation dosimetry in thyroid cancer patients. *J Nucl Med.* 2017;58(10):1666-1671.

## SUPPORTING INFORMATION

Additional supporting information may be found online in the Supporting Information section at the end of this article.

**How to cite this article:** Ostrominski JW, Yada RC, Sato N, et al. CRISPR/Cas9-mediated introduction of the sodium/iodide symporter gene enables noninvasive in vivo tracking of induced pluripotent stem cell-derived cardiomyocytes. *STEM CELLS Transl Med.* 2020;9:1203–1217. <https://doi.org/10.1002/sctm.20-0019>